Supporting Information

Manipulation of Transition Metal Migration via Cr-doping for Better-performance Li-rich Co-free Cathodes

Yameng Fan[a,b], Emilia Olsson[c,d], Bernt Johannessen[e], Anita M. D'Angelo[e], Lars Thomsen[e], Bruce Cowie[e], Lachlan Smillie[f], Gemeng Liang[g], Yaojie Lei[a], Guyue Bo[a], Yunlong Zhao[h], Wei Kong Pang[a*], Qiong Cai[b*], and Zaiping Guo[a,g*]

[a] Institute for Superconducting & Electronic Materials, University of Wollongong, NSW 2500, Australia

[b] School of Chemistry and Chemical Engineering, University of Surrey, Guildford GU2 7XH, United Kingdom

[c] Advanced Research Center for Nanolithography, Amsterdam 1098 XG, The Netherlands

[d] Institute for Theoretical Physics, University of Amsterdam, Amsterdam 1098 XH, The Netherlands

[e] Australian Synchrotron, Australian Nuclear Science and Technology Organization, Clayton Victoria 3168, Australia

[f] Electron Microscopy Centre, University of Wollongong, NSW 2500, Australia

[g] School of Chemical Engineering & Advanced Materials, The University of Adelaide, Adelaide, SA 5005, Australia

[h] School of Design Engineering, Imperial College London, London SW7 2BX, United Kingdom

*Email: wkpang@uow.edu.au (Wei Kong Pang); q.cai@surrey.ac.uk (Qiong Cai); zaiping.guo@adelaide.edu.au (Zaiping Guo).

Experimental Section

Material Synthesis: The carbonate precursor of $Li_{1.2}Ni_{0.2}Mn_{0.6}O_2$ (LNMO) was synthesized via a co-precipitation process. Stoichiometric amounts of $NiSO_4 \cdot 6H_2O$ and $MnSO_4 \cdot H_2O$ were dissolved in deionized water. The salt solution, 2M Na_2CO_3 as precipitator, and 0.3 M NH_4OH as a chelating agent were separately pumped into a continuously stirred reactor tank. The mixed solutions were maintained at a PH of 8.0-8.5 at 55 °C by adjusting the feeding speed of the NH_4OH solution. After formation, the carbonate precursor powder was washed three times with deionized water and dried at 80 °C for 12 h. To obtain pristine LNMO, the carbonate precursor was fully mixed with Li_2CO_3 (5% excess) and calcined at 450 °C for 5 h and 900 °C for 12 h in air. After quenching to room temperature, pristine LNMO was obtained. Cr-LNMO was synthesized with the same process except for adding an appropriate amount of $Cr(NO_3)_3 \cdot H_2O$ to prepare the carbonate precursor. Cr-doped $Li_{1.2}Ni_{0.2}Mn_{0.6}O_2$ are referred to as CLNMO.

Electrochemical Testing: Electrochemical performance was estimated by assembling the active materials into CR2032-type coin cells with lithium metal as the counter electrode. To prepare the cathodes, the active materials were mixed with polyvinylidene difluoride (PVDF) and carbon black (super P) in a weight ratio of 8:1:1 with the solvent of N-methyl-2-pyrrolidone (NMP). A homogeneous slurry was obtained after fully mixing those materials. The obtained slurry was evenly applied onto an aluminium foil and then dried in a vacuum oven (120 °C overnight) to remove the solvents. The dried electrodes were cut into chips with a diameter of 0.6 mm. The average loading mass of the active materials is approximately 2 mg cm^{-2}. The assembly of the coin cells was carried out in an argon-filled glove box with both H_2O and O_2 less than 0.1 ppm. 1 M $LiPF_6$ dissolved in ethylene carbonate and dimethyl carbonate (1:1 vol%) was used as the electrolyte, while Celgard 2400 polypropylene film was the separator.

Galvanostatic charge/discharge testing was carried out on a LAND CT-2001A instrument at ambient temperature. Cyclic voltammetry (CV) and electrochemical impedance spectroscopy (EIS) were collected on a Biologic VMP3 electrochemical workstation. The scanning range of CV was between 2.0 V and 4.8 V. EIS was collected with a disturbance amplitude of 5 mV between 100 kHz and 10 mHz.

Material Characterizations: Lab-based X-ray powder diffraction (XRPD) characterizations were performed on a PANalytical Aeris instrument with Cu Kα radiation. Neutron powder diffraction (NPD) data were collected on the high-resolution neutron powder diffractometer Echidna,[1] at the Open Pool Australian Light Water (OPAL) research at the Australian Nuclear Science and Technology Organisation (ANSTO). The NPD data were recorded in the 2θ range of 4-164° at a step size of 0.05°

with a wavelength of 1.6223(5) Å, using the $La^{11}B_6$ National Institute of Standards and Technology standard reference material 660b. Joint Rietveld refinement based on the XRPD and NPD data was performed using GSAS-II software.[2]

X-ray photoelectron spectroscopy (XPS) data were collected using a Thermo Scientific Nexsa X-ray photoelectron spectrometer system. Calibration was applied to the XPS binding energy using C 1*s* peak (284.8 eV). XPS data were recorded after etching the samples for 300s using an Ar ion gun with an energy of 4000 eV. Scanning electron microscopy (SEM, JEOL JSM 7500) and aberration-corrected transmission electron microscopy (TEM, JEOL ARM-200F) were utilized to study the morphology of the active materials. Energy dispersive spectroscopy (EDS) and scanning TEM high-angle annular dark-field (STEM HAADF) were adopted to investigate the elemental distribution and crystal structure using JEOL ARM-200F at 200 kV. Inductively coupled plasma-atomic emission spectroscopy (ICP-AES) data was collected with Agilent 5800 ICP-OES,

Ex-situ near-edge X-ray fine structure (NEXAFS) characterizations were carried out at the soft X-ray beamline,[3] Australian Synchrotron, Melbourne, Australia. To measure the active materials at different states of charge/discharge, cycled coin cells were disassembled in an argon-filled glove box and then the cycled electrodes were obtained and sealed in a vacuum bag to transfer for the characterizations. The NEXAFS data were analysed using Igor Pro 8, with the QANT[4] add-in developed by the scientists at the Australian Synchrotron. The X-ray absorption (XAS) data were collected at the XAS beamline of the Australian Synchrotron. The XAS data were processed using Athena.[5]

Operando XRPD measurements were carried out at the Powder Diffraction beamline at the Australian synchrotron. The details of the *operando* XRPD experiments have been provided in our group's previous work.[6] An MYTHEN II detector with a continuous acquisition time of 60s was used to collect the data.[7] The wavelength is 0.688762(1) Å confirmed by using the $La^{11}B_6$ National Institute of Standards and Technology standard reference material 660b. The batteries were charged/discharged at the current density of 0.1 C and 0.2 C during the first and the 200th cycle, respectively, with a voltage window between 2.0 and 4.8 V.

Computational Methods: The periodic spin-polarised DFT simulations were conducted using the Vienna Ab Inito Simulation Package (VASP) version 6.3.2.[8-13] After convergence tests to ensure convergence at 1 meV/atom, the plane wave cut-off was set at 800 eV and the k-spacing to 0.3.[14] All simulations were performed using the Perdew-Burke-Ernzserhof (PBE) functional, with the projector-augmented wave method (PAW) used to describe the ion-electron interaction with electronic and ionic

self-consistence force convergence criteria of 10^{-5} eV and 10^{-3} eV/Å. The DFT+U method was applied to account for the d-electrons with U_{eff} for Cr being 3.5, Mn 5.1 and Ni 6.5.[12, 13, 15]

The simulation cells were generated based on the experimentally obtained structures (Table S2 and S3), and enumerated using the supercell programme to probe the relative stability between the different site occupancy factors. The lowest energy structures are presented in supporting information in Figure S15. The undoped hexagonal structure consisted of 48 atoms (12 Li, 4 Ni, 8 Mn, and 24 O), and has lattice parameters 6.04 Å, 6.00 Å, and 14.65 Å. The undoped monoclinic simulation cell contained 96 atoms (32 Li, 16 Mn, and 48 O) with lattice parameters 10.01 Å, 8.65 Å, and 9.71 Å, and beta angle 99.6°. These lattice parameters are in excellent agreement with the experimentally measured ones. To obtain the inequivalent CLNMO structures, the Site-Occupance Disorder Programme (SOD) was used.[16] To calculate the dopant formation energies, the defect formation energy approach by Northrup and Zhang was used, taking the chemical potential references from the metallic bulks.[17] Using SOD, we enumerated the inequivalent sites for Cr-substitution Mn, Ni, and Li sites and geometry optimised each dopant structure. To study the delithiated structure, all Li were removed from the monoclinic structure, and the simulation cell was geometry optimised to account for any relaxations as a function of the vacant Li sites, where after single Cr dopants were placed on the octahedral (previous Li, and substitutional Mn) and tetrahedal (previously occupied by Li in the lithiated cell) sites, respectively, and the full structure geometry optimised.

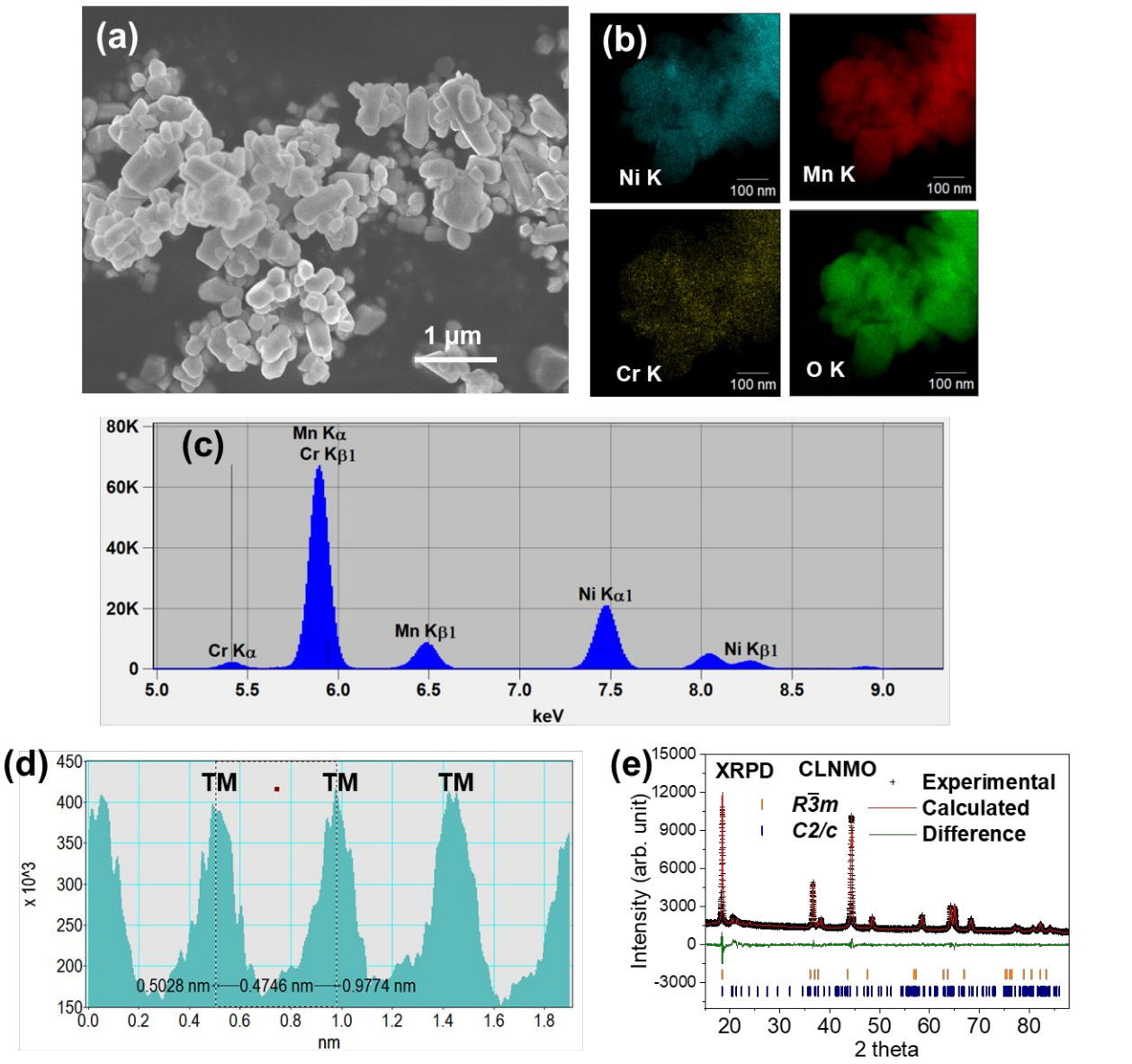

Figure S1. (a) SEM image of CLNMO. (b) Elemental mapping images of Ni, Mn, Cr, and O in CLNMO correponding to the TEM image in Figure 1a. (c) EDS spectrum of CLNMO. (d) Line profile analysis along the blue line in Figure 1b. (f) XRPD of CLNMO used for joint Rietveld refinement profiles.

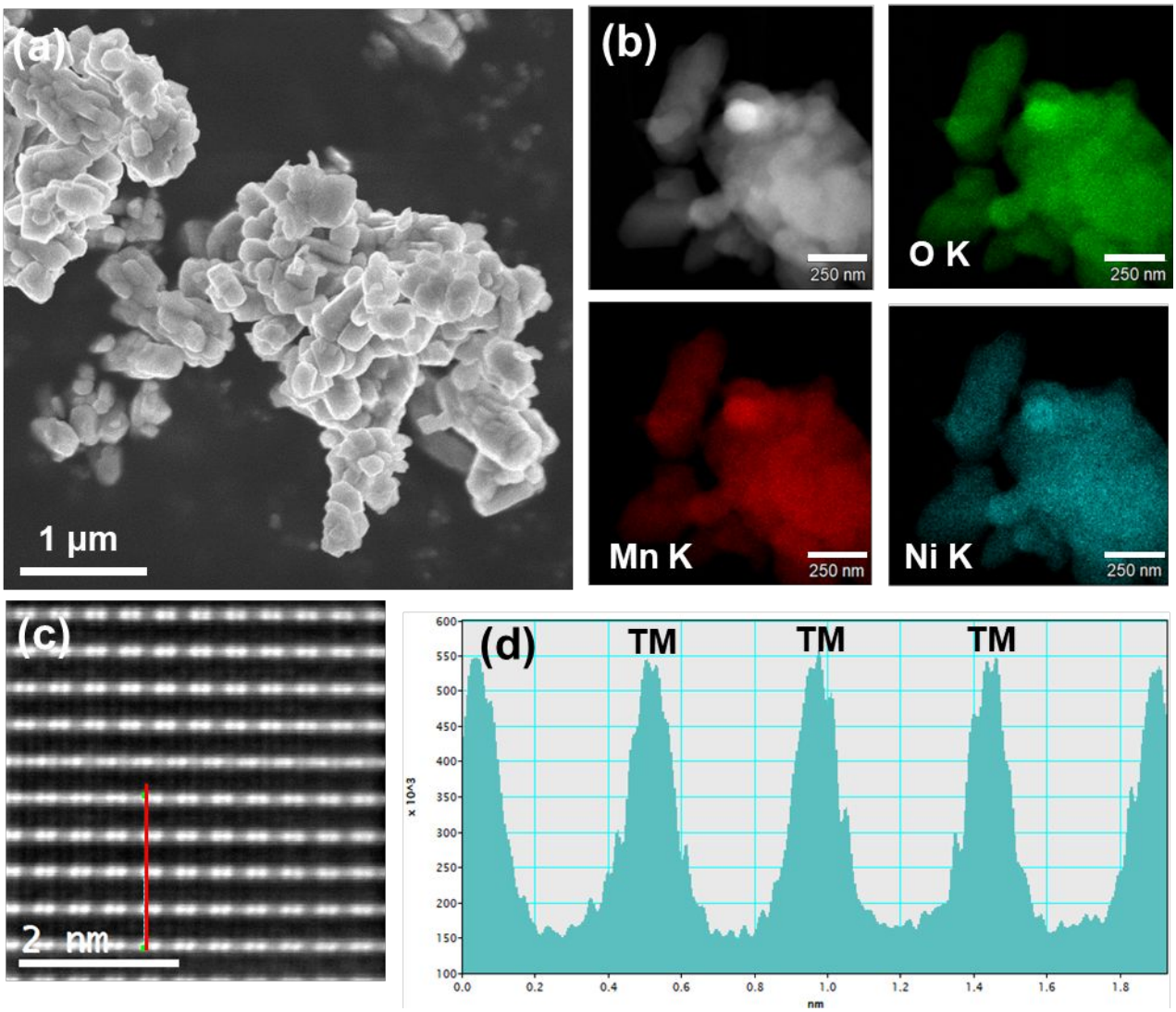

Figure S2. (a) SEM and (b) TEM images and the corresponding elemental mapping images of the LNMO. (c) HAADF STEM images and (d) the corresponding line profile analysis along the red line in (c).

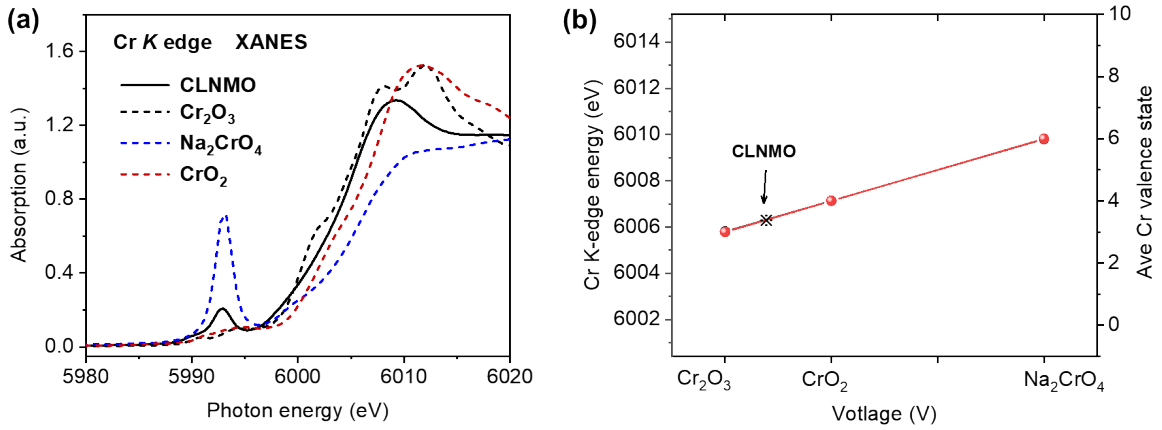

Figure S3. (a) Cr K edge XANES spectra of Cr_2O_3, Na_2CrO_4, and the CLNMO. (b) Cr K edge positions and the average Cr valence states of Cr_2O_3, CrO_2, and Na_2CrO_4.

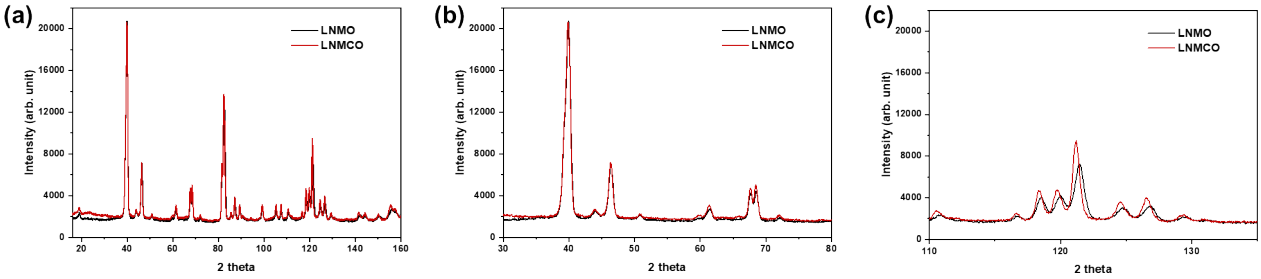

Figure S4. The comparison of the NPD data of LNMO and CLNMO.

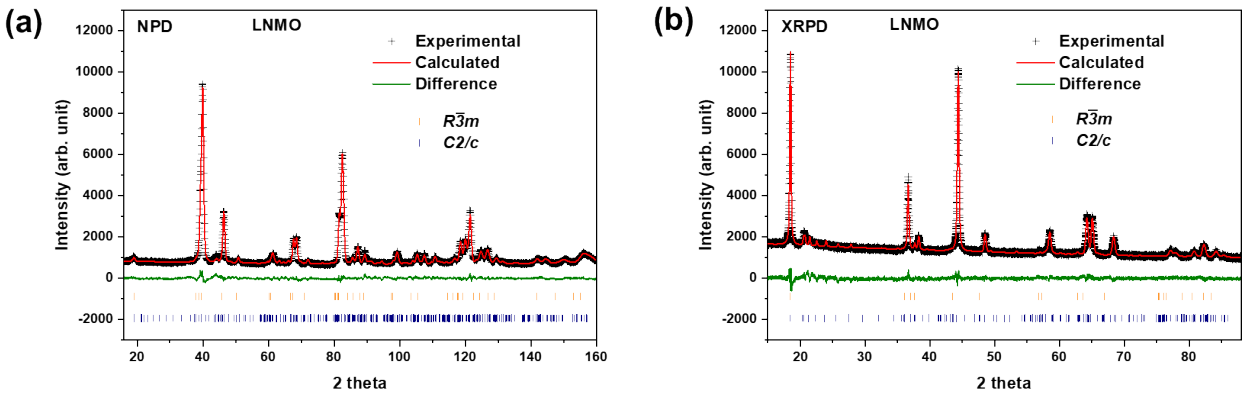

Figure S5. Joint Rietveld refinement profiles using (a) NPD and (b) XRPD data of LNMO (R_{wp} = 4.53%, GOF = 1.79, *C*2/*c* = 61(1) wt%, $R\bar{3}m$ = 39(1) wt%).

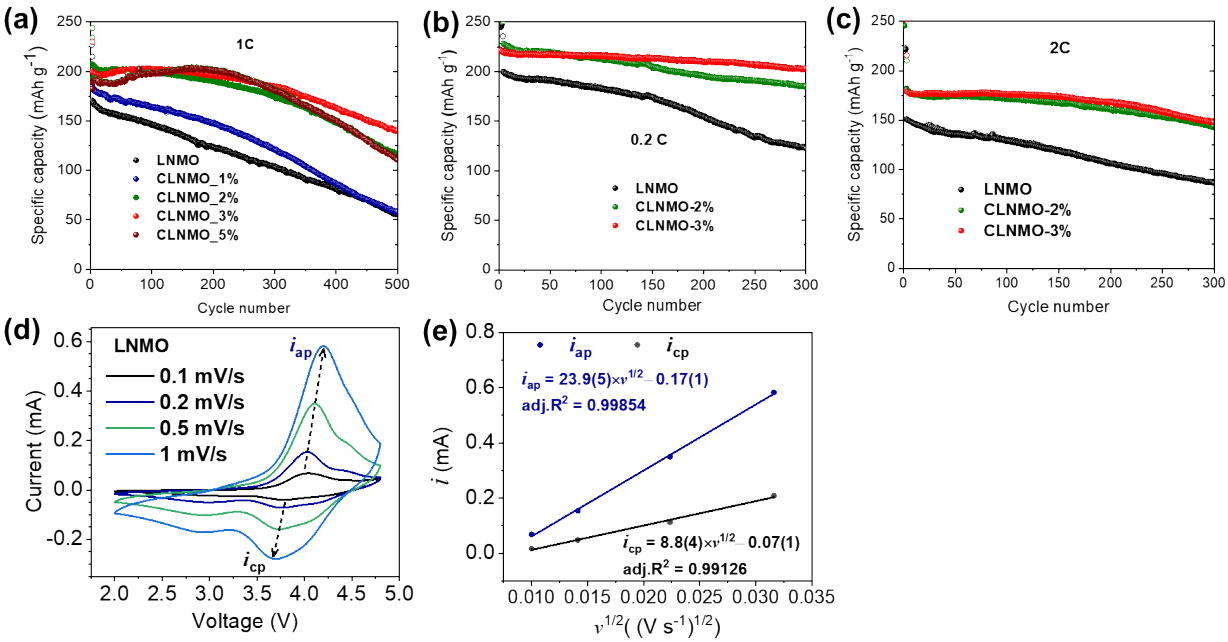

Figure S6. Cycling performance of different samples at (a) 1C, (b) 0.2 C and (c) 2 C. CV curves of (d) LNMO at different scanning rates. Current peak as a function of square root of scan rate of (e) LNMO.

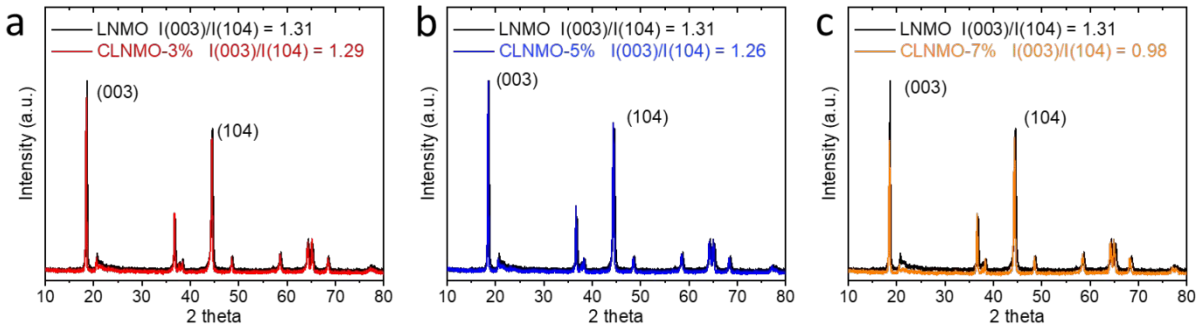

Figure S7. Comparison of the XRD patterns of LNMO and the CLNMO with different doping content. I(003)/I(104) denotes the intensity ratio of the reflection peaks of (003) and (104).

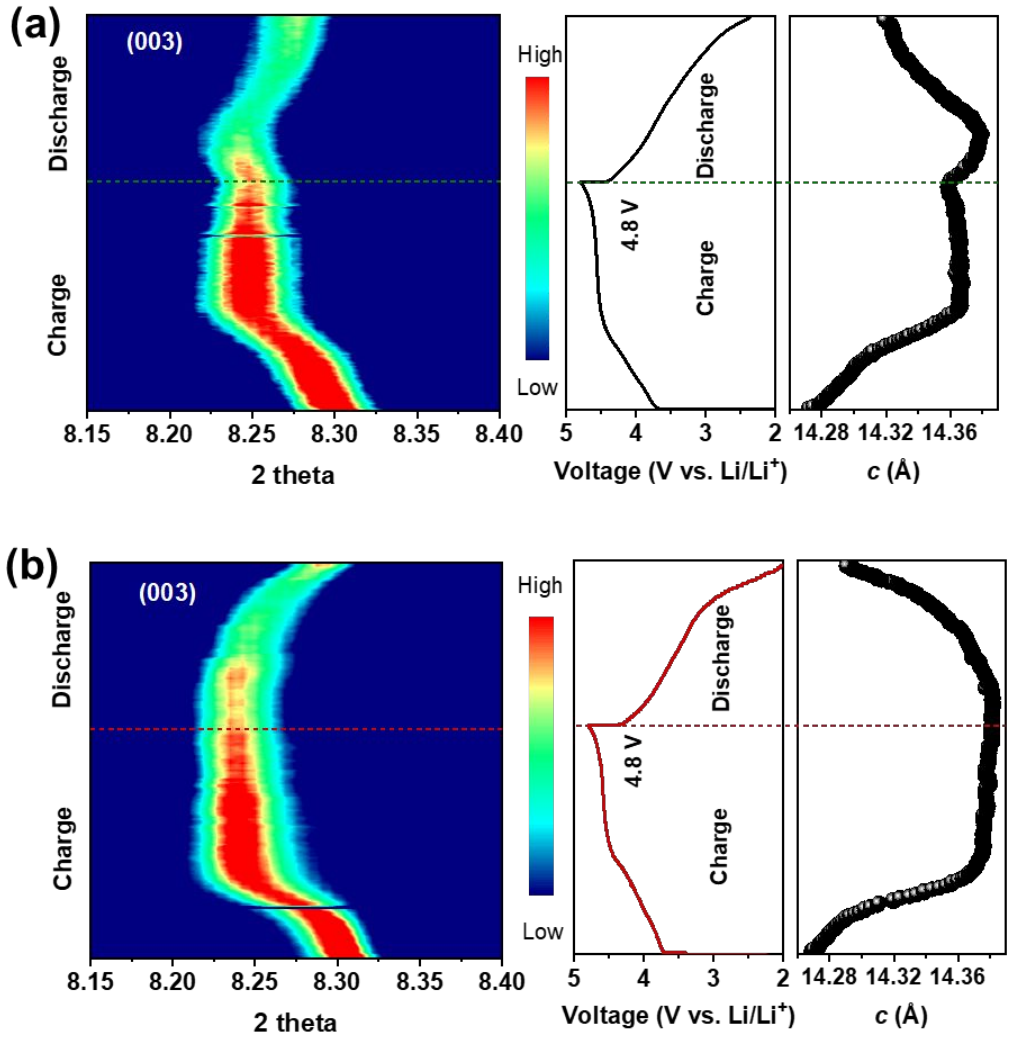

Figure S8. Contour plot of *operando* synchrotron XRPD data and corresponding single peak fitting results and electrochemical curves of cells containing (a) LNMO and (b) CLNMO at the first cycle in a selected 2 theta range.

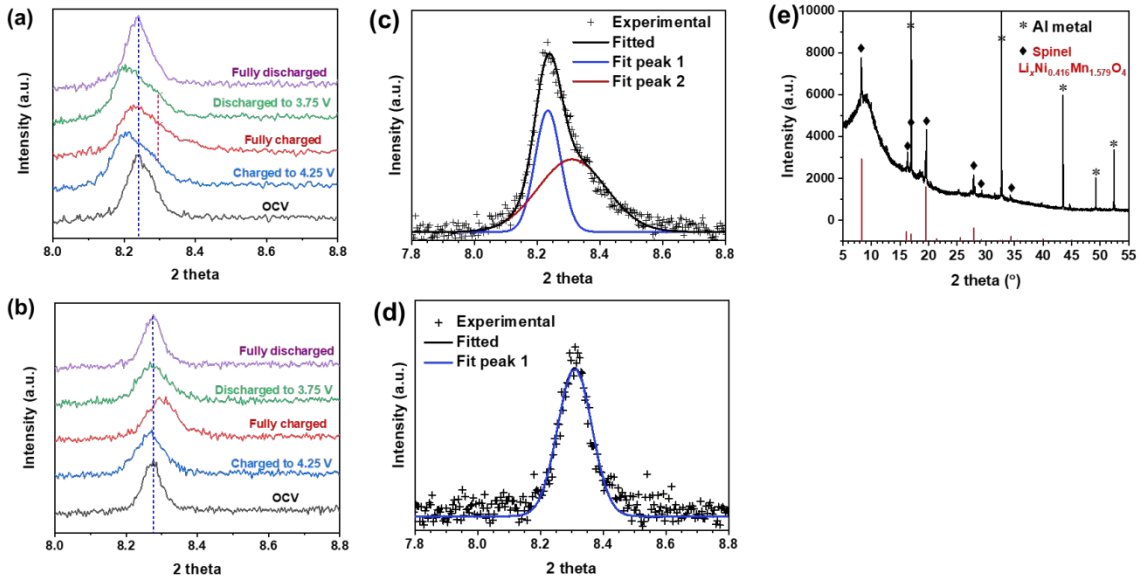

Figure S9. The comparison of the 103 reflection of (a) LNMO and (b) CLNMO at different charge/discharge states with the new reflection marked with a red dash line. The single peak fitting results of (c) LNMO and (d) CLNMO at the fully charged state (4.8 V). (e) In-situ XRD pattern at fully charged state (4.8V) with reflections in red lines corresponding to spinel $Li_xNi_{0.416}Mn_{1.579}O_4$ ($0 < x \leq 1$).

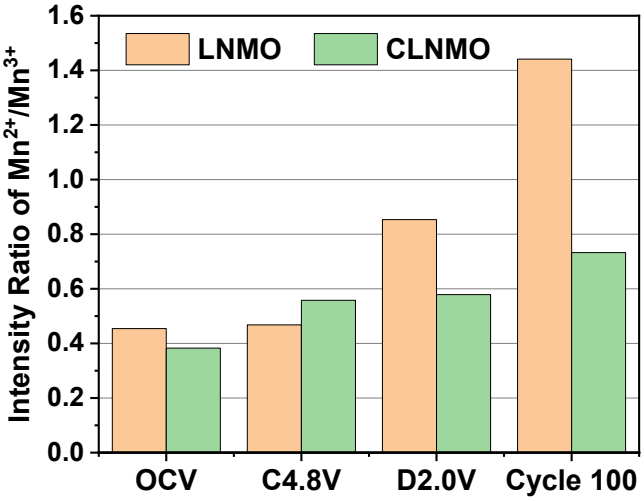

Figure S10. Comparison of the intensity ratio between Mn^{2+} and Mn^{3+}.

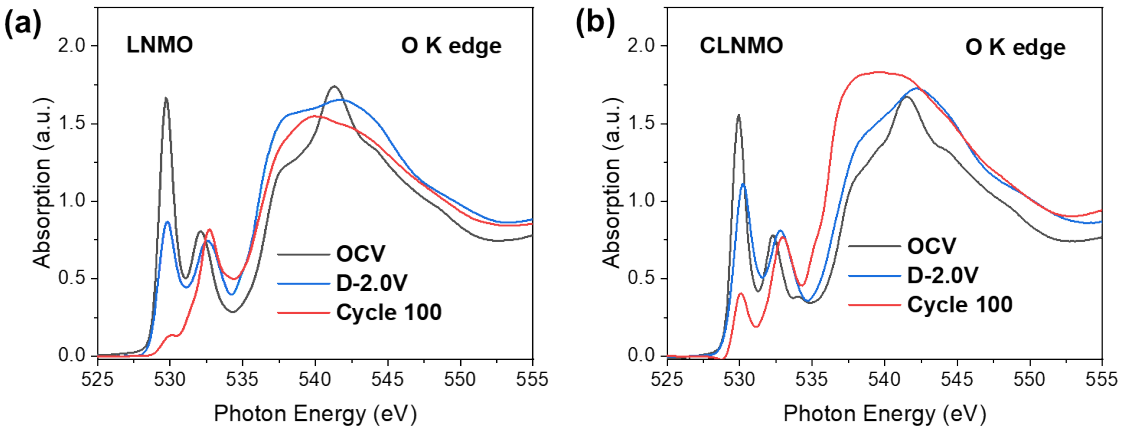

Figure S11. O K edge spectra of the (a) LNMO and (b) CLNMO.

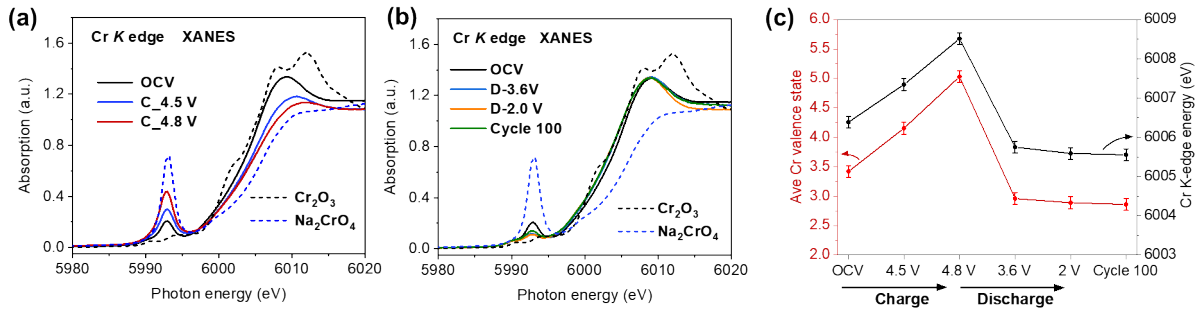

Figure S12. (a, b) Cr K edge XANES spectra of Cr_2O_3, Na_2CrO_4, and the CLNMO at different charge/discharge states. (c) Cr K edge positions and the average Cr valence states determined by averaging the linear rising edge of the Cr K edge XANES spectra.

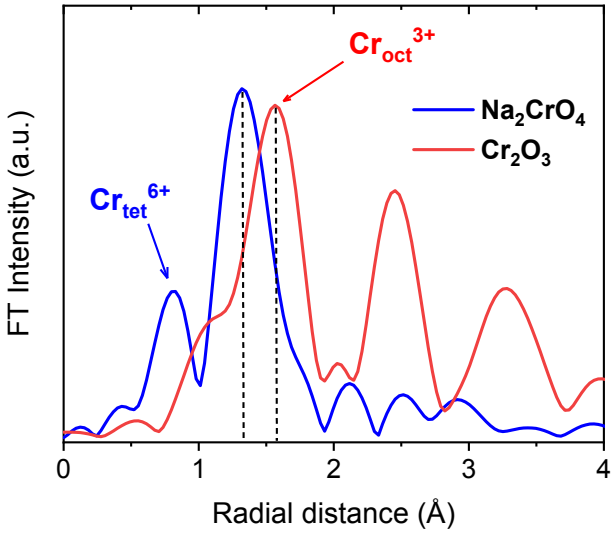

Figure S13. k^2-weightd Cr K edge EXAFS spectra of Na_2CrO_4 and Cr_2O_3.

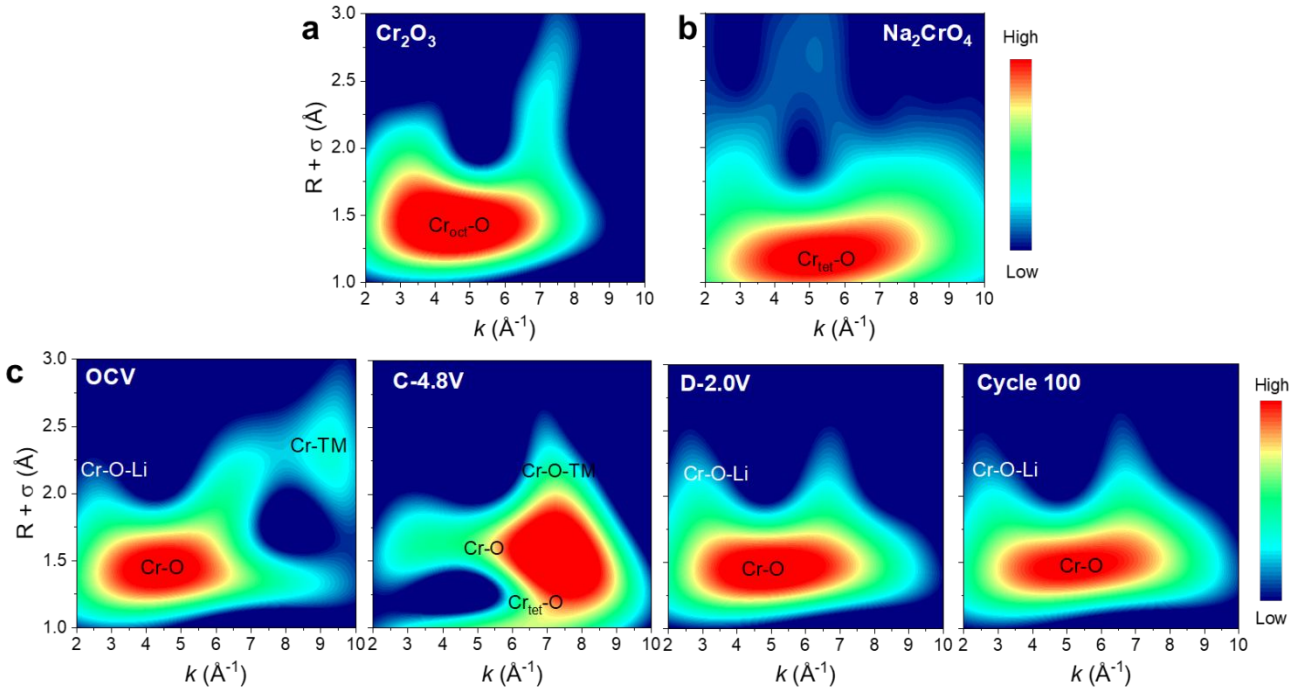

Figure S14. Morlet wavelet transforms of k^2-weightd Cr K edge EXAFS spectra of (a) Cr_2O_3 (with Cr in octahedra) and (b) Na_2CrO_4 (with Cr in tetrahedra). (c) Morlet wavelet transform of the k^2-weighted Cr K edge EXAFS spectra of CLNMO at different states. The C-4.5V, C-4.8 V, D-2.0 V, and Cycle 100 represent the states of charging to 4.5 V, fully charging to 4.8 V, and fully discharging to 2.0 V in the first cycle, and discharging to 2.0 V in the 100th cycle, respectively

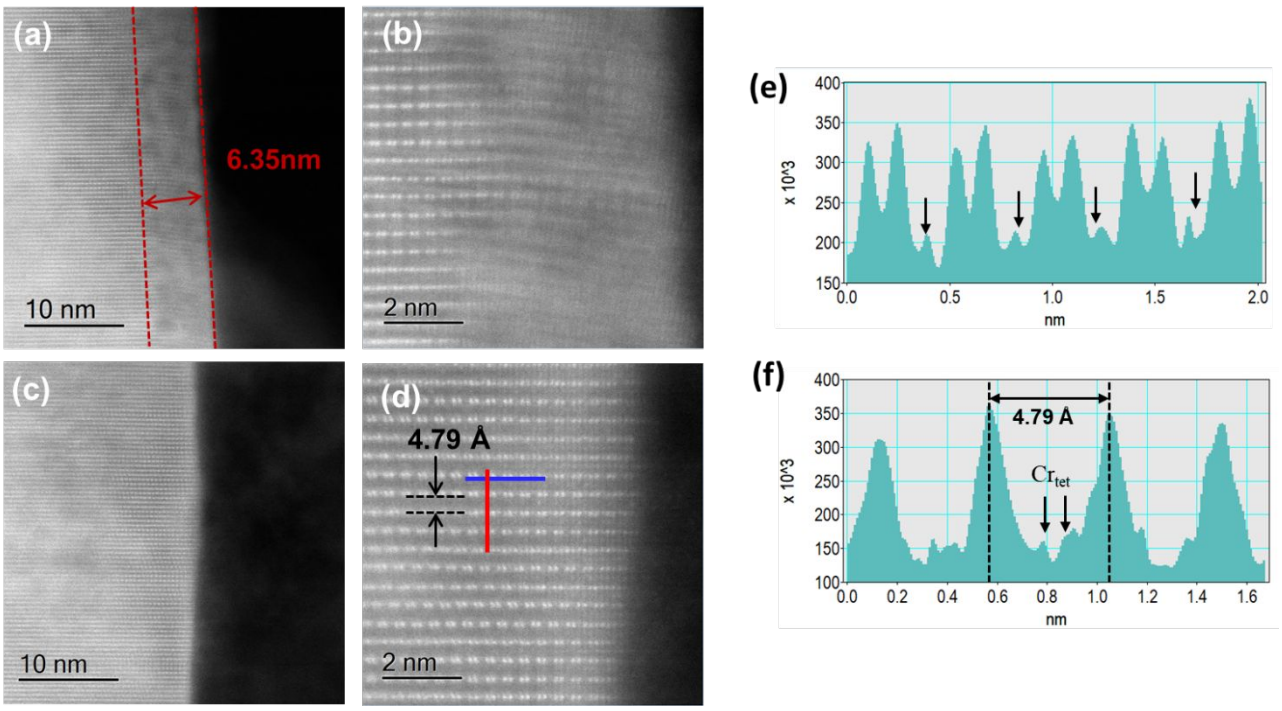

Figure S15. HAADF STEM images of (a, b) LNMO and (c, d) CLNMO at fully delithiated state. (e) and (f) line profile analysis along the blue and red lines in (d), respectively.

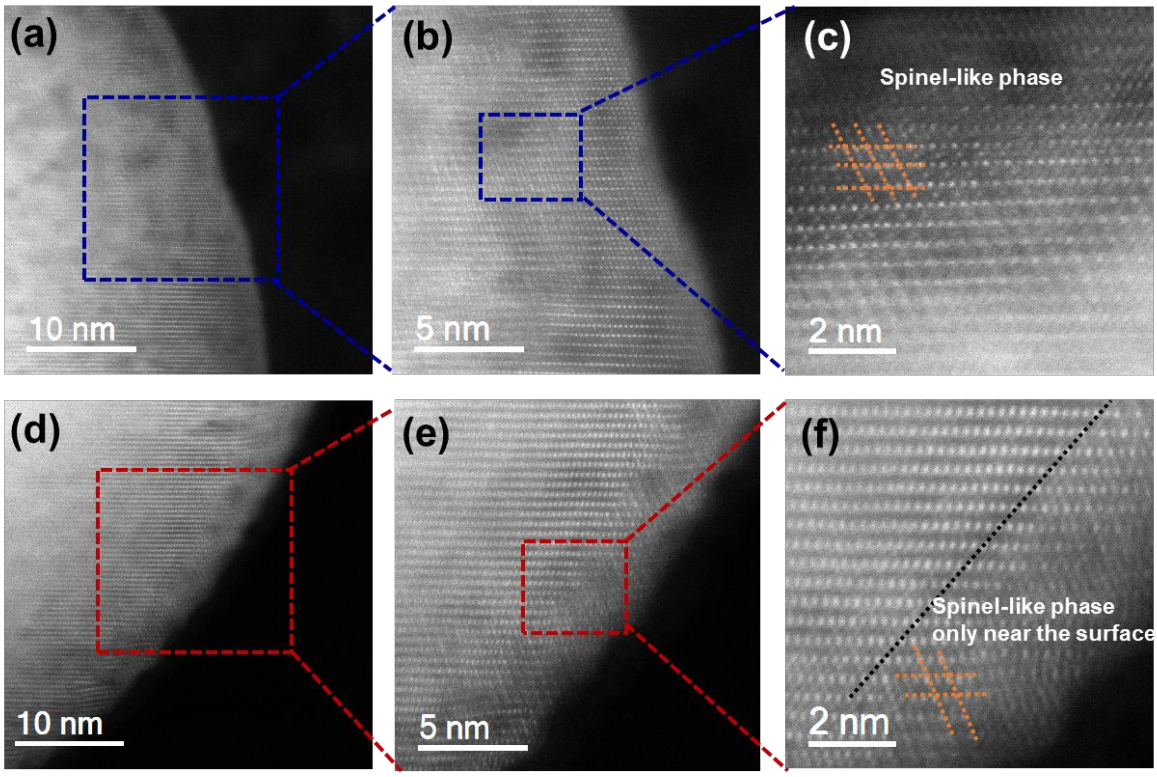

Figure S16. Different-magnification HAADF STEM images of (a-c) LNMO and (d-f) CLNMO after 100 cycles. The cycled LNMO has more spinel-like domains than the cycled CLNMO.

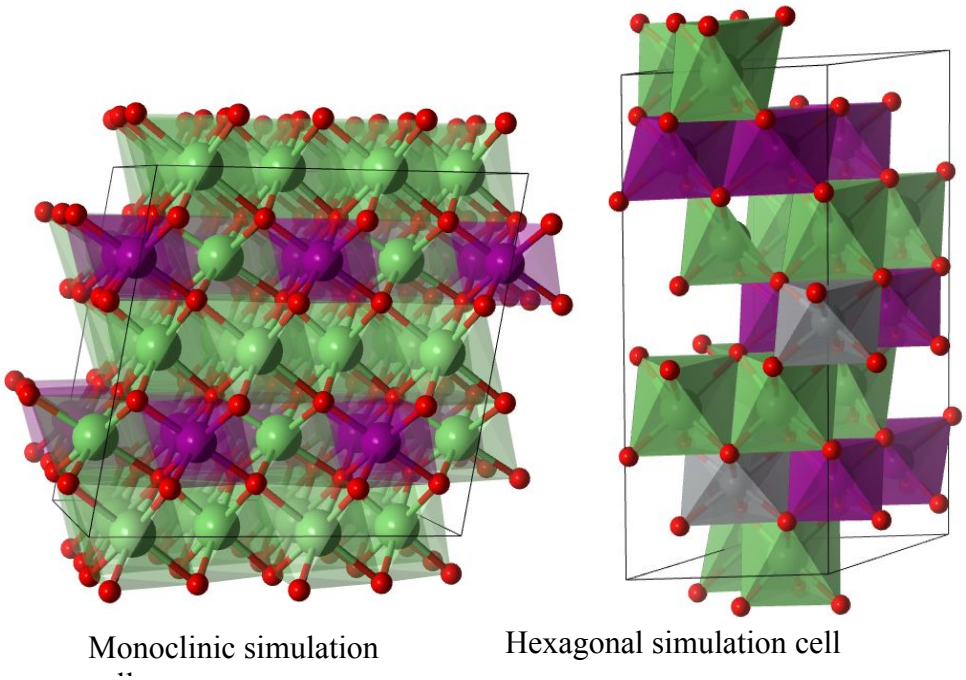

Figure S17. Polyhedral view of the optimized lowest energy configurations. Green represents Li, purple Mn, grey Ni, and red O. Both structural illustrations were generated with VESTA.[18]

Table S1. ICP-AES analysis data for the atomic compositions of LNMO and CLNMO.

Samples		Measured Element (Molar ratio)			
		Li	Ni	Mn	Cr
LNMO	$Li_{1.2}Ni_{0.2}Mn_{0.6}O_2$	1.19(1)	0.20(1)	0.59(1)	\
CLNMO_1%	$Li_{1.2}Ni_{0.2}Mn_{0.59}Cr_{0.01}O_2$	1.21(1)	0.20(1)	0.58(1)	0.01(1)
CLNMO_3%	$Li_{1.2}Ni_{0.2}Mn_{0.58}Cr_{0.02}O_2$	1.21(1)	0.20(1)	0.58(1)	0.03(1)
CLNMO_5%	$Li_{1.2}Ni_{0.2}Mn_{0.55}Cr_{0.05}O_2$	1.22(1)	0.20(1)	0.54(1)	0.04(1)

Table S2. Crystallography details and phase composition and of CLNMO obtained from joint Rietveld refinement using NPD and XRPD data.

CLNMO (R_{wp} = 4.78%, GOF = 1.95)							
Phase1	**Hexagonal *R*-3*m* phase (37(1) wt%)**						
	***a*/Å**			***c*/Å**		**Volume/Å^3**	
	2.8570(2)			14.2617(8)		100.820(8)	
	Atom	**Wyckoff site**	***x***	***y***	***z***	**U_{iso} (Å^2)**	**Site occupancy factor**
	Li1	3*b*	0.00000	0.00000	0.00000	0.0100	0.942(4)
	Ni1	3*b*	0.00000	0.00000	0.00000	0.0100	0.058(4)
	Li2	3*a*	0.00000	0.00000	0.50000	0.0136(12)	0.080
	Ni2	3*a*	0.00000	0.00000	0.50000	0.0136(12)	0.371(5)
	Mn2	3*a*	0.00000	0.00000	0.50000	0.0136(12)	0.569(5)
	Cr2	3a	0.00000	0.00000	0.50000	0.0136(12)	0.025
	O	6*c*	0.00000	0.00000	0.2377 (3)	0.0196(10)	1
Phase2	**Monoclinic *C2/c* phase (63(1) wt%)**						
	***a*/Å**	***b*/Å**		***c*/Å**	**beta/^{o}**	**Volume/Å^3**	
	4.9569(4)	8.5839 (4)		9.6362(10)	99.6726(30)	404.187(15)	
	Atom	**Wyckoff site**	***x***	***y***	***z***	**U_{iso} (Å^2)**	**Site occupancy factor**
	Li1	8*f*	0.3292(27)	0.0843(20)	0.0391(13)	0.0154	1
	Li2	4*d*	0.25000	0.25000	0.50000	0.0154	1
	Li3	4*e*	0.00000	0.7182(12)	0.25000	0.0087(7)	0.630(10)
	Mn3	4*e*	0.00000	0.7175(11)	0.25000	0.0087(7)	0.370(10)
	Mn4	4*e*	0.00000	0.4231(10)	0.25000	0.0087(7)	1
	Mn5	4*e*	0.00000	0.0836(14)	0.25000	0.0087(7)	0.535(14)
	Li5	4*e*	0.00000	0.0836(14)	0.25000	0.0087(7)	0.445(14)
	Cr5	4*e*	0.00000	0.0836(14)	0.25000	0.0087(7)	0.025
	O1	8*f*	0.1032(7)	0.2532(9)	0.1372(4)	0.0009(3)	1
	O2	8*f*	0.1354(10)	0.5781(7)	0.1277(5)	0.0009(3)	1
	O3	8*f*	0.1331(11)	0.9328(7)	0.1318(5)	0.0009(3)	1

In the hexagonal phase, the Li/Ni mixing was considered. Li1 and Ni1 were constrained to be equal, while Li2, Ni2, Mn2 and Cr2 were constrained to be equal. Given the challenges posed by the considerable overlap between hexagonal and monoclinic phases, the collected NPD data, with a limited Q range (up to 7.6 Å^{-1}) and spatial resolution, exhibit restricted sensitivity to the influences of occupancy and Uiso values, particularly when refined simultaneously. To circumvent the generation of inconclusive outcomes, we imposed constraints on Uiso for each phase and refined the occupancies accordingly. In the monoclinic phase, the Uiso of Li1 and Li2 was constrained to be equal, while the Uiso of Li3, Mn3, Mn4, Mn5, Li5, and Cr5 was constrained to be equal. The refinement takes no account of the Cr_{tet} due to its very low content in the pristine state, less than 0.5%.

Table S3. Crystallography details and phase composition of LNMO obtained from joint Rietveld refinement using NPD and XRPD data.

LNMO (R_{wp} = 4.53%, GOF = 1.79)							
Phase1	**Hexagonal *R*-3*m* phase (39(1) wt%)**						
	***a*/Å**			***c*/Å**		**Volume/Å^3**	
	2.8588(2)			14.2468(9)		100.841(8)	
	Atom	**Wyckoff site**	***x***	***y***	***z***	**U_{iso} (Å^2)**	**Site occupancy factor**
	Li1	3*b*	0.00000	0.00000	0.00000	0.0142	0.910(4)
	Ni1	3*b*	0.00000	0.00000	0.00000	0.0142	0.090(4)
	Li2	3*a*	0.00000	0.00000	0.50000	0.0129(16)	0.080
	Ni2	3*a*	0.00000	0.00000	0.50000	0.0129(16)	0.362(4)
	Mn1	3*a*	0.00000	0.00000	0.50000	0.0129(16)	0.558(4)
	O	6*c*	0.00000	0.00000	0.24044	0.0087(6)	1
Phase2	**Monoclinic *C*2/*c* phase (61(1) wt%)**						
	***a*/Å**	***b*/Å**	***c*/Å**	**beta/º**	**Volume/Å^3**		
	4.9520(5)	8.5671(5)	9.6332(16)	99.647(5)	402.861(22)		
	Atom	**Wyckoff site**	***x***	***y***	***z***	**U_{iso} (Å^2)**	**Site occupancy factor**
	Li1	8*f*	0.3017(44)	0.0874(19)	0.0238(19)	0.0021(1)	1
	Li2	4*d*	0.25000	0.25000	0.50000	0.0021(1)	1
	Li3	4*e*	0.00000	0.7358(17)	0.25000	0.0027(9)	0.602(9)
	Mn3	4*e*	0.00000	0.7358(17)	0.25000	0.0027(9)	0.398(9)
	Mn4	4*e*	0.00000	0.4178(11)	0.25000	0.0027(9)	1
	Mn5	4*e*	0.00000	0.0793(15)	0.25000	0.0027(9)	0.578(11)
	Li5	4*e*	0.00000	0.0793(15)	0.25000	0.0027(9)	0.422(11)
	O1	8*f*	0.1032(11)	0.2547(9)	0.1346(6)	0.0039(5)	1
	O2	8*f*	0.1360(11)	0.5637(7)	0.1301(6)	0.0039(5)	1
	O3	8*f*	0.1549(15)	0.9249(7)	0.1353(6)	0.0039(5)	1

The same constraints were imposed as those applied in the refinement of CLNMO.

Table S4. The lithium diffusion coefficient calculated by Randles-Sevcik equation[19, 20].

Sample	**LNMO**		**CLNMO**	
Peak	**Anodic**	**Cathodic**	**Anodic**	**Cathodic**
$i/(v^{1/2})$ **(A/((Vs^{-1})$^{1/2}$))**	0.0304(8)	0.0239(5)	0.0088(4)	0.0134(10)
Lithium diffusion coefficient D_{Li} (cm^2 s^{-1})	$4.1(2)\times10^{-11}$	$2.6(1)\times10^{-11}$	$3.4(4)\times10^{-12}$	$8.0(12)\times10^{-12}$

Randles-Sevcik equaltion[19, 20] can be described as:

$$i_p = k \cdot n^{3/2} \cdot \mathrm{A} \cdot C \cdot D^{1/2} \cdot v^{1/2}$$

, where i_p represents the peak current (A), constant $k = 2.69 \times 10^5$ when the temperature is 298.15 K, n is the number of exchanged electrons, A is the electrode surface area (cm^2), C is the bulk concentration of charge charriers (mol cm^{-3}), D is diffusion coefficient (cm^2 s^{-1}), and v is canning rate (Vs^{-1}).

Table S5. Capacity retention comparison of CLNMO with other previously reported Co-free LLOs.

Cathode Material	Current Rate (mA g^{-1})	Initial Discharge Capacity (mAh g^{-1})	Cycles	Capacity Retention	Mass Loading (mg cm^{-1})	Ref.
Surface-Fe-doped $Li_{1.2}Mn_{0.56}Ni_{0.24}O_2$	250	200	300	86.4%	/	[21]
Zr-doped $Li_{1.2}Ni_{0.2}Mn_{0.6}O_2$	250	180	300	92%	2–3	[22]
Nb-doped $Li_{1.2}Ni_{0.27}Mn_{0.53}O_2$	250	212	200	86%	/	[23]
$Li_{1.2}Mn_{0.585}Ni_{0.185}Fe_{0.03}O_2$	250	160	200	80%	/	[24]
Layered-spinel-heterostructure-coated $Li_{1.2-\sigma}Mn_{0.6}Ni_{0.2}O_2$	250	200	200	84%	/	[25]
$LiMn_{0.8}Fe_{0.2}PO_4$/C-blended $Li_{1.2}Ni_{0.2}Mn_{0.6}O_2$	250	160	500	81%	/	[26]
Fe-doped $Li_{1.2}Ni_{0.2}Mn_{0.6}O_2$	250	159	500	76.8%	1–2	[27]
Cl-doped $Li_{1.2}Ni_{0.2}Mn_{0.6}O_2$	250	155	500	65.7%		
Fe/Cl-doped $Li_{1.2}Ni_{0.2}Mn_{0.6}O_2$	250	184	500	86.4%		
Surface-modified $Li_{1.2}Ni_{0.2}Mn_{0.6}O_2$ with a spinel phase and Co gradient doping	250	210	200	91%	~2	[28]
CO_2/urea-treated $Li_{1.2}Ni_{0.2}Mn_{0.6}O_2$	200	200	200	77.2%	~2	[29]
Li_2SiO_3-coated $Li_{1.13}Ni_{0.3}Mn_{0.57}O_2$	200	165	100	90%	/	[30]
Hierarchical porous $Li_{1.17}Ni_{0.25}Mn_{0.58}O_2$	125 (0.5C)	231	200	94%	~3	[31]
CLNMO	**250**	**200**	**200**	**99%**	~2	**This work**
			300	**92%**		
			500	**71%**		

Reference

1. Liss, K.-D.; Hunter, B.; Hagen, M.; Noakes, T.; Kennedy, S., Echidna—the new high-resolution powder diffractometer being built at OPAL. *J. Phys. Condens. Matter* **2006,** *385-386*, 1010-1012.
2. Toby, B. H.; Von Dreele, R. B., GSAS-II: the genesis of a modern open-source all purpose crystallography software package. *J. Appl .Crystallogr.* **2013,** *46* (2), 544-549.
3. Cowie, B. C. C.; Tadich, A.; Thomsen, L., The current performance of the wide range (90‐2500 eV) soft X‐ray beamline at the Australian Synchrotron. *AIP Conf. Proc.* **2010,** *1234* (1), 307-310.
4. Gann, E.; McNeill, C. R.; Tadich, A.; Cowie, B. C. C.; Thomsen, L., Quick AS NEXAFS Tool (QANT): a program for NEXAFS loading and analysis developed at the Australian Synchrotron. *J. Synchrotron Radiat.* **2016,** *23* (1), 374-380.
5. Ravel, B.; Newville, M., ATHENA, ARTEMIS, HEPHAESTUS: data analysis for X-ray absorption spectroscopy using IFEFFIT. *J. Synchrotron Radiat.* **2005,** *12* (4), 537-541.
6. Liang, G.; Hao, J.; D'Angelo, A. M.; Peterson, V. K.; Guo, Z.; Pang, W. K., A robust coin-cell design for in situ synchrotron-based X-ray powder diffraction analysis of battery materials. *Batter. Supercaps* **2021,** *4* (2), 380-384.
7. Wallwork, K. S.; Kennedy, B. J.; Wang, D., The high resolution powder diffraction beamline for the Australian Synchrotron. *AIP Conf. Proc.* **2007,** *879* (1), 879-882.
8. Kresse, G.; Hafner, J., Ab initio molecular dynamics for liquid metals. *Phys. Rev. B* **1993,** *47* (1), 558.
9. Kresse, G.; Hafner, J., Ab initio molecular-dynamics simulation of the liquid-metal–amorphous-semiconductor transition in germanium. *Phys. Rev. B* **1994,** *49* (20), 14251.
10. Kresse, G.; Furthmüller, J., Efficiency of ab-initio total energy calculations for metals and semiconductors using a plane-wave basis set. *Comput. Mater. Sci.* **1996,** *6* (1), 15-50.
11. Kresse, G.; Furthmüller, J., Efficient iterative schemes for ab initio total-energy calculations using a plane-wave basis set. *Phys. Rev. B* **1996,** *54* (16), 11169.
12. Kresse, G.; Joubert, D., From ultrasoft pseudopotentials to the projector augmented-wave method. *Phys. Rev. B* **1999,** *59* (3), 1758.
13. Blöchl, P. E., Projector augmented-wave method. *Phys. Rev. B* **1994,** *50* (24), 17953.
14. Monkhorst, H. J.; Pack, J. D., Special points for Brillouin-zone integrations. *Phys. Rev. B* **1976,** *13* (12), 5188.
15. Perdew, J. P.; Burke, K.; Ernzerhof, M., Generalized gradient approximation made simple. *Phys. Rev. Lett* **1996,** *77* (18), 3865.
16. Grau-Crespo, R.; Hamad, S.; Catlow, C. R. A.; De Leeuw, N., Symmetry-adapted configurational modelling of fractional site occupancy in solids. *J. Phys. Condens. Matter* **2007,** *19* (25), 256201.
17. Zhang, S.; Northrup, J. E., Chemical potential dependence of defect formation energies in GaAs: Application to Ga self-diffusion. *Phys. Rev. Lett.* **1991,** *67* (17), 2339.
18. Momma, K.; Izumi, F., VESTA 3 for three-dimensional visualization of crystal, volumetric and morphology data. *J. Appl. Crystallogr.* **2011,** *44* (6), 1272-1276.
19. Ottmann, A.; Zakharova, G.; Ehrstein, B.; Klingeler, R., Electrochemical performance of single crystal belt-like NH4V3O8 as cathode material for lithium-ion batteries. *Electrochim. Acta* **2015,** *174*, 682-687.
20. Liang, G.; Olsson, E.; Zou, J.; Wu, Z.; Li, J.; Lu, C. Z.; D'Angelo, A. M.; Johannessen, B.; Thomsen, L.; Cowie, B.; Peterson, V. K.; Cai, Q.; Pang, W. K.; Guo, Z., Introducing 4s-2p orbital hybridization to stabilize spinel oxide cathodes for lithium-ion batteries. *Angew. Chem. Int. Ed.* **2022**, e202201969.
21. Ye, Z.; Zhang, B.; Chen, T.; Wu, Z.; Wang, D.; Xiang, W.; Sun, Y.; Liu, Y.; Liu, Y.; Zhang, J.; Song, Y.; Guo, X., A Simple Gas–Solid Treatment for Surface Modification of Li-Rich Oxides Cathodes. *Angew. Chem. Int. Ed.* **2021,** *60* (43), 23248-23255.
22. Zhang, J.; Zhang, Q.; Wong, D.; Zhang, N.; Ren, G.; Gu, L.; Schulz, C.; He, L.; Yu, Y.; Liu, X., Addressing voltage decay in Li-rich cathodes by broadening the gap between metallic and anionic bands. *Nat. Commun.* **2021,** *12* (1), 3071.
23. Zhang, C.; Wei, B.; Jiang, W.; Wang, M.; Hu, W.; Liang, C.; Wang, T.; Chen, L.; Zhang, R.; Wang, P.; Wei, W., Insights into the enhanced structural and thermal stabilities of Nb-substituted lithium-rich layered oxide cathodes. *ACS Appl. Mater. Interfaces* **2021,** *13* (38), 45619-45629.

24. Wu, F.; Kim, G. T.; Diemant, T.; Kuenzel, M.; Schür, A. R.; Gao, X.; Qin, B.; Alwast, D.; Jusys, Z.; Behm, R. J., Reducing capacity and voltage eecay of Co‐free $Li_{1.2}Ni_{0.2}Mn_{0.6}O_2$ as positive electrode material for lithium batteries employing an ionic liquid‐based electrolyte. *Adv. Energy Mater.* **2020,** *10* (34), 2001830.
25. Zhang, Y.; Shi, X.; Zheng, S.; Ouyang, Y.; Li, M.; Meng, C.; Yu, Y.; Wu, Z.-S., Alternate heterogeneous superlattice control of lattice strain to stabilize Li-rich cathode. *Energy Environ. Sci.* **2023**.
26. Han, C.; Wu, J.; Li, S.; Li, T.; Li, J.; Liu, H., Suppressing the voltage decay of $Li_{1.2}Mn_{0.6}Ni_{0.2}O_2$ cathode materials enabled by $LiMn_{0.8}Fe_{0.2}PO_4$/C for long-cycling lithium-ion batteries. *Solid State Ion.* **2021,** *364*, 115629.
27. Nie, L.; Wang, Z.; Zhao, X.; Chen, S.; He, Y.; Zhao, H.; Gao, T.; Zhang, Y.; Dong, L.; Kim, F.; Yu, Y.; Liu, W., Cation/Anion Codoped and Cobalt-Free Li-Rich Layered Cathode for High-Performance Li-Ion Batteries. *Nano Letters* **2021,** *21* (19), 8370-8377.
28. Liu, H.; Xiang, W.; Bai, C.; Qiu, L.; Wu, C.; Wang, G.; Liu, Y.; Song, Y.; Wu, Z.-G.; Guo, X., Enabling superior electrochemical performance of lithium-rich $Li_{1.2}Ni_{0.2}Mn_{0.6}O_2$ cathode materials by surface integration. *Ind. Eng. Chem. Res.* **2020,** *59* (43), 19312-19321.
29. Bao, L.; Wei, L.; Fu, N.; Dong, J.; Chen, L.; Su, Y.; Li, N.; Lu, Y.; Li, Y.; Chen, S., Urea-assisted mixed gas treatment on Li-rich layered oxide with enhanced electrochemical performance. *J. Energy Chem.* **2022,** *66*, 123-132.
30. Zhao, E.; Liu, X.; Zhao, H.; Xiao, X.; Hu, Z., Ion conducting Li_2SiO_3-coated lithium-rich layered oxide exhibiting high rate capability and low polarization. *Chem. Commun.* **2015,** *51* (44), 9093-9096.
31. Chen, M.; Jin, X.; Chen, Z.; Zhong, Y.; Liao, Y.; Qiu, Y.; Cao, G.; Li, W., A cross-like hierarchical porous lithium-rich layered oxide with (110)-oriented crystal planes as a high energy density cathode for lithium ion batteries. *J. Mater. Chem. A* **2019,** *7* (21), 13120-13129.